JOURNAL OF APPLIED PHYSICS **113**, 084303 (2013)

Monte Carlo study of electron-beam penetration and backscattering in multi-walled carbon nanotube materials: The effect of different scattering models

Ioanna Kyriakou,[1] Dimitris Emfietzoglou,[1,a)] Alireza Nojeh,[2] and Marko Moscovitch[3]
[1]*Medical Physics Lab, University of Ioannina Medical School, 451 10 Ioannina, Greece*
[2]*Department of Electrical and Computer Engineering, The University of British Columbia, Vancouver, British Columbia V6T 1Z4, Canada*
[3]*Department of Radiation Medicine, Georgetown University Medical Center, Washington DC, NW 20057, USA*

(Received 16 January 2013; accepted 30 January 2013; published online 25 February 2013)

A systematic study of electron-beam penetration and backscattering in multi-walled carbon nanotube (MWCNT) materials for beam energies of ~0.3 to 30 keV is presented based on event-by-event Monte Carlo simulation of electron trajectories using state-of-the-art scattering cross sections. The importance of different analytic approximations for computing the elastic and inelastic electron-scattering cross sections for MWCNTs is emphasized. We offer a simple parameterization for the total and differential elastic-scattering Mott cross section, using appropriate modifications to the Browning formula and the Thomas-Fermi screening parameter. A discrete-energy-loss approach to inelastic scattering based on dielectric theory is adopted using different descriptions of the differential cross section. The sensitivity of electron penetration and backscattering parameters to the underlying scattering models is examined. Our simulations confirm the recent experimental backscattering data on MWCNT forests and, in particular, the steep increase of the backscattering yield at sub-keV energies as well as the sidewalls escape effect at high-beam energies. © *2013 American Institute of Physics*. [http://dx.doi.org/10.1063/1.4792231]

I. INTRODUCTION

Studies on the interaction of electron beams with CNTs are important for understanding the mechanism of image formation and damage in electron microscopy,[1,2] as well as for advancing efforts to tailor their properties via e-beam assisted modification.[3,4] Furthermore, the potential use of CNTs in nanodevices that will be used in radiation rich environments, such as those encountered in space[5] or in nuclear technology applications[6] (including medicine[7]) necessitates that their response to a variety of ionizing radiation fields be well understood. Other applications of the interaction of electrons with CNTs could be in vacuum nanoelectronic devices for electron multiplication and amplification[8] or in X-ray generators for medical imaging. Such interactions can also provide useful information on the properties of the material itself through techniques such as electron energy-loss spectroscopy.[9] An important consideration in all the above studies is that, given the small interaction volume that nanostructures provide for fast-moving electrons, there might be fundamental differences in how these interactions take place in CNTs versus bulk materials. The study of CNTs in this context may thus have important implications for other nanomaterials (nanowires and nanoparticles) as well.

Monte Carlo (MC) simulation is a well-established technique for studying electron-beam penetration, energy deposition, transmission, backscattering, and secondary emission in both bulk matter and solid surfaces.[10] However, the simulation of the complex electron trajectories in matter crucially depends upon the theoretical models used to compute elastic and inelastic electron-scattering cross sections.

At present, the default version of most MC electron transport codes in arbitrary solids (e.g., DJ,[11] CASINO,[12] WinX,[13] NISTMonte[14]) uses the so-called continuous-slowing-down-approximation (CSDA), whereby the energy-loss resulting from inelastic collisions in-between individual elastic scattering events is simulated from stopping-power theory. For relatively high-energy electrons (above ~10 keV), Bethe's stopping-power formula and the screened Rutherford elastic-scattering cross section offer a rather accurate and computationally efficient description of electron transport within the CSDA scheme. Their extension to lower energies is commonly made using semi-empirical modifications such as the Joy–Luo[15] stopping-power formula and the Browning[16] elastic model, among others.[17,18] However, it is now recognized that for sub-keV electron transport down to the backscattering ~50 eV or secondary emission ~1-10 eV cut-offs or for materials which cannot be considered "bulk" (i.e., practically unbounded), one must switch from a continuous- to a discrete-energy-loss model as well as replace the Rutherford model by partial-wave calculations of the Mott cross section.[19,20]

The first MC studies of backscattering and secondary emission for CNTs were carried out by the Nojeh group (UBC code).[21,22] Specifically, backscattering was originally simulated[21] within the CSDA using the Joy–Luo and Browning models, while in a follow-up study,[22] that included secondary emission, a discrete-energy-loss model was implemented based on binary-collision models of inelastic scattering and a

[a)]Author to whom correspondence should be addressed. Electronic mail: demfietz@cc.uoi.gr.

simplified electron-gas description for (undamped) plasmon excitations. Material characteristics specific to the MWCNT forests were implemented at the level of elastic scattering by fitting the results to experimental backscattering data. Such a "hybrid" approach whereby the contribution of different inelastic channels is computed from separate theories (first introduced by the Osaka group[23] and also used in the MONSEL[24] code) offers a viable alternative to CSDA at low energies. Self-consistency is often invoked by a comparison of the energy-loss rate (computed from the partial inelastic scattering cross sections) against the Joy-Luo stopping power formula.

Recently, the inelastic scattering of low-energy electrons (<30 keV) in CNTs was studied using a dielectric response function determined from experimental optical data and appropriate dispersion relations[25,26] and, along with the original Browning model,[27] was implemented in a homemade MC code to simulate electron transport and energy dissipation in MWCNT materials.[28] The use of a discrete-energy-loss model based on a semi-empirical dielectric response function is presently considered the state-of-the-art for low-energy electron transport in bulk solids and solid surfaces, because it offers a realistic description of the electronic excitations of the material with single-particle and plasmon losses computed self-consistently (under the constraint of sum-rules) within a single model.[29–32] Furthermore, in place of an undamped plasmon (used in both the UBC[22] and MONSEL[24] codes), more realistic models that account for plasmon dispersion and lifetime broadening can be included. A low-energy improvement of the Joy-Luo formula based on experimental optical data for the dielectric response function is also available as a separate routine in CASINO,[33] whereas a simple δ-oscillator description of the dielectric response function underlines inelastic scattering in the PENELOPE[34] code.

In the present work, we investigate the influence of different scattering models on the MC simulation of electron-beam penetration and backscattering in MWCNT materials for energies that cover both (ultra-) low-voltage ($\sim$0.1 to $\sim$5 keV) and conventional ($\sim$5-30 keV) scanning electron microscopy (SEM) irradiation conditions. We provide analytic parameterizations of the total and differential elastic-scattering Mott cross-sections of NIST[35] which presently represents the most accurate partial-wave calculations publicly available.[36] A discrete-energy-loss approach to inelastic scattering is adopted, using different analytic approximations for the differential cross section of MWCNTs obtained from dielectric theory. A comparison of our results with recent experimental data on MWCNT forests is presented.

All scattering models presented are in their non-relativistic form which is a standard approximation for the present energy range where relativistic corrections are practically inconsequential. For the inclusion of relativistic effects in electron scattering, one may consult the comprehensive treatment of Fernández-Varea and co-workers.[37]

II. METHODOLOGY

A. Elastic scattering models

The most popular elastic scattering models in electron transport simulations assume that the interaction of electrons with the target nuclei is mediated by an exponentially-screened Coulomb potential (also known as Wentzel model) of the form

$$V(r) = -\frac{Ze^2}{r}\exp\left(-\frac{r}{R_s}\right), \tag{1}$$

where Z is the atomic number of the target atom and R_s is a model-dependent screening radius that is commonly expressed in terms of the Thomas-Fermi (TF) screening length, a_{TF}, as

$$R_s = \frac{a_{\mathrm{TF}}}{\tau}, \tag{2}$$

where $a_{\mathrm{TF}} = 0.885 a_{\mathrm{B}} Z^{-1/3}$ with a_{B} denoting the Bohr radius, and τ is a low-energy correction factor (to be discussed below). The main advantage of the Wentzel model, Eq. (1), is that, within the first Born approximation, both the differential cross section (DCS) and the total cross section (TCS) for elastic scattering can be expressed analytically as follows:[10]

$$\frac{d\sigma_{el}}{d\Omega} = \frac{Z^2 e^4}{4T^2}\frac{1}{(1-\cos\theta+2n)^2}, \tag{3}$$

where $d\Omega = 2\pi \sin\theta d\theta$ and

$$\sigma_{el} = \int \frac{d\sigma_{el}}{d\Omega} d\Omega = \frac{Z^2 e^4}{4T^2}\frac{\pi}{n(n+1)}, \tag{4}$$

where T is the electron kinetic energy and n is the so-called screening parameter. The latter depends on the screening radius, R_s, through:

$$n = \frac{1}{4}\left(\frac{\hbar}{q_0}\right)^2 R_s^{-2} \tag{5}$$

with q_0 the electron momentum before the collision. So, the choice of the screening parameter, n, essentially depends upon the choice of τ. Setting $\tau = 1$ results in the Thomas-Fermi screening parameter:

$$n_{\mathrm{TF}} = 4.34\frac{Z^{2/3}}{T}. \tag{6}$$

Two other common approximations for the screening parameter are those of Bishop[11] (after setting $\tau = 0.885$)

$$n_{\mathrm{B}} = 3.4\frac{Z^{2/3}}{T} \tag{7}$$

and Nigam[38,39] (after setting $\tau = 1.12$)

$$n_{\mathrm{N}} = 5.44\frac{Z^{2/3}}{T}. \tag{8}$$

In the literature, Eqs. (3) and (4) are known as the *screened Rutherford* formulae, and due to the fact that they are based on the first Born approximation, their use is mostly justified at relatively high energies and low-Z materials. Nevertheless, owing to their computational simplicity, their usage is commonly extended even down to sub-keV energies.

A more accurate approach to elastic electron scattering at low energies is to use the so-called Mott cross-section that is derived from elaborate partial-wave calculations.[35] However, due to their numerical form, the implementation of Mott cross section data is demanding (and inconvenient), so many authors have looked for ways to represent them in an approximate manner through analytical functions. Perhaps the most notable of such efforts is due to Browning *et al.*,[16,27] who suggested a simple semi-analytic elastic scattering model that was deduced from inspection of known trends of the Mott cross section. In its latest version the elastic TCS is given by the formula[16]

$$\sigma_{\text{Brown.}} = \frac{3\times 10^{-18} Z^{1.7}}{(T + 0.005\, Z^{1.7} T^{0.5} + 0.0007\, Z^2/T^{0.5})}, \quad (9)$$

where $\sigma_{\text{Brown.}}$ is in cm^2 and T in keV. On the other hand, the elastic DCS is decomposed into two parts, one being the same with the screened Rutherford model and another that assumes an isotropic distribution. The ratio of the Rutherford-to-isotropic scattering cross section is given by[16]

$$\frac{\sigma_{\text{Ruth.}}}{\sigma_{\text{isotr.}}} = \frac{300\, T}{Z} + \frac{Z^3}{3\times 10^5 T}, \quad (10)$$

which gives the same forward-to-backscattered ratio, $f/b = \int_0^{90}(d\sigma/d\theta)d\theta \div \int_{90}^{180}(d\sigma/d\theta)d\theta)$, as the Mott cross section. In this scheme, the oscillatory features of the differential Mott cross section are averaged out and a smooth angle dependence is obtained.

In Figs. 1 and 2, we compare the results of the above models with the NIST[35] data for atomic carbon that are derived from accurate partial-wave calculations of the Mott cross section within the static-exchange approximation using a Dirac-Hartree-Fock potential. Although the NIST data are strictly valid for free atoms, they are considered reliable even for solids down to ~200 eV (or lower) and currently represent the state-of-the-art in elastic-scattering Mott cross sections.[36] In comparison, the most frequently cited earlier Mott cross sections of Reimer and Lodding[40] and Czyzewski *et al.*[41] either neglect exchange or are based on the less accurate Thomas-Fermi-Dirac (or Hartree-Fock) potential, respectively. As explained elsewhere,[36] low-energy corrections to the NIST data (e.g., for polarization effects) would predominantly affect small-angle scattering which, in the context of penetration and backscattering, is less critical than large-angle scattering that would remain, to a good approximation, unaffected. Note that the comparison of the elastic DCS in Fig. 2 is made indirectly through the elastic transport cross section,

$$\sigma_{tr} = 2\pi \int_0^{\pi} (1-\cos\theta)\frac{d\sigma_{el}}{d\Omega}\sin\theta\, d\theta, \quad (11)$$

which provides a weighted average of the angular deflection in elastic scattering and, therefore, is a more pertinent parameter for transport calculations than the elastic DCS.[35]

With respect to the elastic TCS (Fig. 1), all the screened Rutherford models underestimate the NIST data at high energies (by up to 50% at 30 keV) and overestimate them at low energies (by up to 80% at 50 eV). The Browning model, on the other hand, provides very good agreement with the NIST data above 1 keV but performs less well at lower energies where differences reach 20-25%. With respect to the elastic transport cross section (Fig. 2), the screened Rutherford model with the Thomas-Fermi screening parameter provides a very good agreement with the NIST data above 1 keV, but

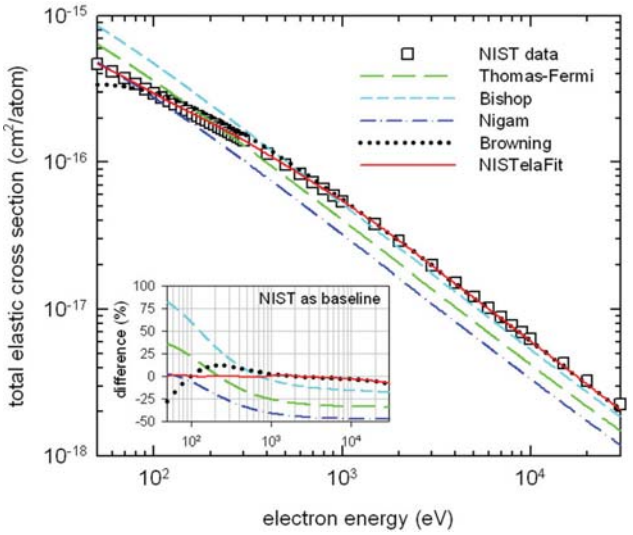

FIG. 1. Total cross section (TCS) for elastic electron scattering with carbon atoms as a function of electron energy. Calculations are based on the screened Rutherford formula, Eq. (4), using Thomas-Fermi, Eq. (6) (long dash), Bishop's Eq. (7) (short dash), and Nigam's Eq. (8) (dash-dot line) screening parameters, the Browning formula Eq. (9) (dotted line), and the present NISTelaFit model of Eqs. (12) and (13) (full line). For comparison, the partial-wave calculations of NIST[35] (box symbol) are also presented. The inset presents the % difference from the NIST data.

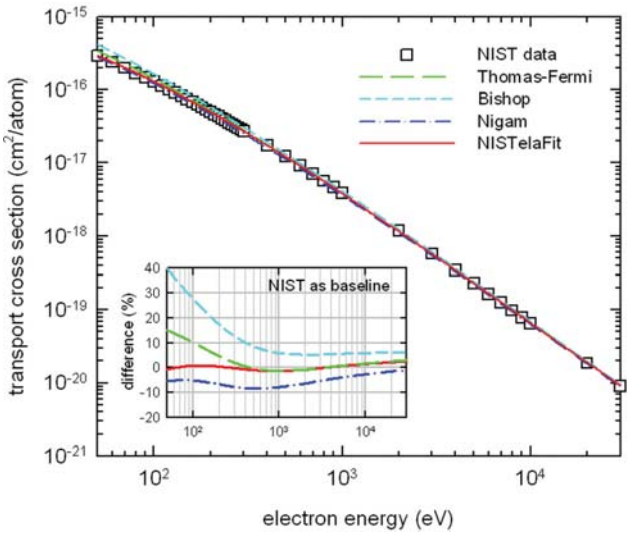

FIG. 2. The transport cross section, Eq. (11), for elastic electron scattering with carbon atoms as a function of electron energy. Calculations are based on the screened Rutherford formula, Eq. (3), using the Thomas-Fermi Eq. (6) (long dash), Bishop's Eq. (7) (short dash), and Nigam's Eq. (8) (dash-dot line) screening parameters, and the present NISTelaFit model of Eqs. (14) and (15) (full line). For comparison, the partial-wave calculations of NIST[35] (box symbol) are also presented. The inset presents the % difference from the NIST data.

it is less satisfactory at lower energies with differences reaching 15% at 50 eV. On the other hand, the use of the Nigam screening parameter underestimates by up to 10%, the NIST data throughout the entire energy range while the Bishop screening parameter leads to even larger deviations. The Browning model is not included in Fig. 2 since its DCS is not analytic.

Motivated by the above results and in order to obtain good agreement with the NIST data for both the total and the transport elastic scattering cross section throughout the entire energy range (i.e., both above and below 1 keV), we suggest the following scheme. For the elastic TCS, we use

$$\sigma_{el} = \begin{cases} \sigma_{\text{Brown.}}, & T \geq 1\,\text{keV}, \\ \sigma_{\text{Brown.}} \times f^{\text{corr.}}_{\text{Brown.}}, & T < 1\,\text{keV}, \end{cases} \tag{12}$$

where $\sigma_{\text{Brown.}}$ is Browning's expression, Eq. (9), and $f^{\text{corr.}}_{\text{Brown.}}$ is a fitting function that "corrects" (towards the NIST data) the Browning model at low energies as follows:

$$f^{\text{corr.}}_{\text{Brown.}} = \frac{\sigma_{\text{NIST}}}{\sigma_{\text{Brown.}}} \approx 0.869 + 1.08 \cdot 10^{-4} T + 2.275 \exp(-0.03T) \tag{13}$$

with T in eV. As it can be seen from Fig. 1, Eqs. (12) and (13) offer an agreement to better than ±3% with the NIST data for the elastic TCS throughout the entire energy range (50 eV – 30 keV). For the elastic DCS, we use:

$$\frac{d\sigma_{el}}{d\Omega} = \begin{cases} \dfrac{d\sigma_{\text{TF}}}{d\Omega}, & T \geq 1\,\text{keV}, \\ \dfrac{d\sigma^{\text{corr.}}_{\text{TF}}}{d\Omega}, & T < 1\,\text{keV}, \end{cases} \tag{14}$$

where $d\sigma_{\text{TF}}/d\Omega$ is the screened Rutherford expression, Eq. (3), with the Thomas-Fermi screening parameter, Eq. (6), and $d\sigma^{\text{corr.}}_{\text{TF}}/d\Omega$ includes an energy-dependent low-energy correction to the TF screening parameter that reads:

$$n_{\text{corr.}} = n_{\text{TF}} \times \tau^2 = n_{\text{TF}} \left\{ 1 + \exp\left(-\frac{T}{200} - 2.15 \right) \right\}^2 \tag{15}$$

with T in eV. Note that Eq. (15) recovers the Thomas-Fermi screening parameter at high energies where $\tau \approx 1$, but is corrected to higher values at low energies where $\tau > 1$ and screening becomes more effective. Although the form of Eq. (15) is similar to the one suggested by Fitting and Reinhardt,[42] the parameters in Eq. (15) have been optimized so that Eq. (14) fits within ±3% the NIST data for the elastic transport cross section throughout the entire range (50 eV–30 keV). The excellent agreement of the present elastic scattering model (hereafter to be called NISTelaFit), Eqs. (12)–(15), with the NIST data for the total and transport elastic scattering cross section is shown in Figs. 1 and 2, respectively.

B. Inelastic scattering models

According to the dielectric theory,[43] the inelastic electron–electron interaction is mediated by a dynamically screened Coulomb potential. Then, in the non-relativistic first Born approximation (or linear response theory), the DCS (per atom) for energy-loss is given by the expression[44]

$$\left.\frac{d\sigma_{inel}}{dE}\right|_{\text{Born}} = \frac{Z}{N\pi a_{\text{B}} T} \int_{q_-}^{q_+} \text{Im}\left\{ -\frac{1}{\varepsilon(E,q)} \right\} \frac{dq}{q}, \tag{16}$$

where $q_\pm = \sqrt{2m}(\sqrt{T} \pm \sqrt{T-E})$ is the minimum (−) and maximum (+) momentum-transfer in the collision, E is the energy loss, m is the electron mass, N is the electron density of the material, and $\varepsilon(E,q)$ is the energy- and momentum-dependent dielectric response function of the medium (here the MWCNT material). The quantity $\text{Im}\{-1/\varepsilon(E,q)\}$ inside the integral is the so-called energy-loss function (ELF), which describes, in the framework of the dielectric theory, the complete (in the E–q plane) electronic excitation spectrum of the material.

Evidently, the integral form of Eq. (16) prohibits its direct use in transport simulations. In addition, handling a large set of numerical data of $d\sigma_{inel}/dE$ vs. E for each electron energy T, is also impractical. Therefore, we have examined two alternative approaches which both retain the central role of the ELF in computing the inelastic DCS. The first approach is inspired by the Bethe theory and is based on replacing the q-dependent ELF, $\text{Im}\{-1/\varepsilon(E,q)\}$, by its optical limit, $\text{Im}\{-1/\varepsilon(E,q=0)\}$. Although this, so-called optical approximation, is essentially a high-energy approximation,[44] its usage is often extended down to low energies[45] given that the q-dependence of the dielectric function (or the ELF) is seldom known for real materials. In this approximation, the sampling of energy loss can then be made through the following *optical* DCS:

$$\left.\frac{d\sigma_{inel}}{dE}\right|_{\text{optical}} \propto \text{Im}\left\{ -\frac{1}{\varepsilon\Big(E, q=0; E_i(0), \Gamma_i(0)\Big)} \right\}. \tag{17}$$

Following Powell,[46] the contribution of valence shells to the ELF of Eq. (17) can be conveniently obtained from experimental optical data (i.e., at vanishing q). The parameters $E_i(0) \equiv E_i(q=0)$ and $\Gamma_i(0) \equiv \Gamma_i(q=0)$ in Eq. (17), loosely associated with the energy and lifetime (or damping), respectively, of the i-th resonance excitation of the system, are determined from experimental optical data for bulk-like MWCNTs[47] using a many-pole plasmon model[48] under the constraints of sum-rules.[49] As discussed elsewhere,[26] the above ELF model is representative of individual *thick* MWCNTs (more than ~15 walls) or bundled MWCNTs, independently of chirality. On the other hand, the K-shell contribution to the ELF of Eq. (17) is deduced[26] from the atomic X-ray attenuation coefficients of the FFAST database[50] of NIST under the approximation $\text{Im}\{-1/\varepsilon\} \approx \text{Im}\{\varepsilon\}$, which assumes that core-shell excitations are "unscreened."

For a more accurate treatment of inelastic electron scattering at low energies, the variation of the screened electron–electron interaction with q should be explicitly considered. However, in order to avoid the explicit integration of ELF over q, we take advantage of the fact that in Eq. (16) the q-dependence of the ELF is weak compared to the

inverse dependence of the inelastic DCS upon q. Therefore, to a first approximation, the ELF can be taken out of the integral and one can then sample the energy loss from an *effective* DCS:

$$\left.\frac{d\sigma_{inel}}{dE}\right|_{\text{effective}} \propto \text{Im}\left\{-\frac{1}{\varepsilon\left(E, q=q_{eff}; E_i(q), \Gamma_i(q)\right)}\right\}. \quad (18)$$

Note that Eq. (18) reduces to Eq. (17) at the optical limit ($q = 0$). So, in contrast to Eq. (17), the effective DCS is computed from a *dispersed* (i.e., non-local) ELF. The use of Eq. (18) obviously requires some additional information, namely, the exact value of q_{eff} and the dispersion relations, $E_i(q)$ and $\Gamma_i(q)$, according to which the ELF will be extended to $q \neq 0$. With respect to q_{eff}, we are guided by the observation that small-q values contribute more than high-q values to the Born DCS (see Eq. (16)); thus, q_{eff} should be of the order of the minimum momentum transfer $q_{\text{min}} \equiv q_-$. We have found that the best agreement (in terms of the spectral distribution of the DCS) between the Born DCS of Eq. (16) and the effective DCS of Eq. (18) is obtained by setting q_{eff} as twice the value of q_{min} which makes q_{eff} be a function of both T and E. The extension of the ELF from $q = 0$ to arbitrary q is far from trivial even within the context of electron-gas theory.[44,51] Therefore, various phenomenological approaches have been suggested for bulk solids.[52–54] To go beyond the conventional schemes for unbounded solids, we employ here our earlier developed "bulk planar surface" (BPS) model,[26] which in the present context reads:

$$E_i(q) = \sqrt{E_{i,0}^2 + \sqrt{\frac{3}{10}}\upsilon_F E_p q + \frac{3}{5}\upsilon_F^2 q^2 + \left(\frac{q^2}{2m}\right)^2}, \quad (19)$$

where $E_p = \text{Ry}(12/r_s^3)^{1/2}$ and $\upsilon_F = (2\text{Ry}/m)^{1/2}(\alpha r_S)^{-1}$ are the plasmon resonance energy and Fermi velocity of the density-equivalent electron gas, respectively, with $r_S = \frac{1}{\alpha_B}\left(\frac{3}{4\pi N}\right)^{1/3}$ the dimensionless one-electron radius and $\alpha = \left(\frac{4}{9\pi}\right)^{1/3} \cong 0.521$. Note that $E_{i,0} \equiv E_i(0)$, while the index i runs over the total number of poles. The BPS model considers in a general manner boundary effects due to the finite lateral size of the MWCNTs, through the linear dispersion term characteristic of a surface plasmon mode. The remaining quadratic and quartic dispersion terms represent, respectively, the bulk plasmon and single-particle excitations of the system. Thus, Eq. (19) provides the correct limits at $q \to 0$ and $q \to \infty$ while having an electron-gas behavior at intermediate q that combines both bulk and surface modes. As shown elsewhere,[26] the BPS model is in fair agreement with recent experimental data[55] for thick MWCNTs at $q \neq 0$. Although the BPS model provides a simple and physically motivated correction to the conventional infinite-medium dispersion models, dimensionality cross-over effects[56] that properly account for the coupling of the transferred wavevector with the MWCNT structure should be included to further improve the simulations at low energies, especially for individual (or aligned) MWCNTs. For the "unscreened" K-shell excitations, Eq. (19) is simplified to

$$E_K(q) = E_{K,0} + \frac{q^2}{2m}. \quad (20)$$

Finally, momentum broadening effects in the ELF resulting from the finite lifetime of plasmon excitations, which are always damped in real materials at any q and are known to be important at low energies, are included through the empirical expression[26]

$$\Gamma_i(q) = \Gamma_{i,0} + \frac{q}{2}\left(\frac{e^2}{\hbar}\right) + \frac{q^2}{2m}, \quad (21)$$

where $\Gamma_{i,0} \equiv \Gamma_i(0)$.

It is important to recognize that, although for simple metals the Lindhard dielectric response function may provide an adequate description, the use of optical data and semi-empirical dispersion relations has the important advantage that the most important features of the electronic excitation spectrum of the *specific* material (here the MWCNTs) over a wide energy-loss range are explicitly considered in the simulation. On the other hand, the partitioning of the energy loss to plasmon or single-particle excitations (the latter potentially leading to secondary electrons) is not a straightforward task within the present model. An approximate scheme has been described elsewhere.[28] However, the details of this procedure are important only for very-low-energy electrons (below ~50 eV), and therefore, they are of little practical significance in the present study.

Although both approximations discussed above have bypassed the numerical integration of Eq. (16), and thus simplified the computational work considerably, here we investigate yet another approximation to the inelastic DCS obtained from dielectric theory that is based on Tougaard's "universal" function[57] for bulk solids. There are two versions of this function, one for metals and one for polymers. The expression for metals is more appropriate in the present study given the metallic nature of MWCNTs, and leads to the following relation:[58]

$$\left.\frac{d\sigma_{inel}}{dE}\right|_{\text{Tougaard}} \propto \frac{B \cdot E}{(C + E^2)^2}, \quad (22)$$

where $B = 2866$ eV^2 and $C = 1643$ eV^2. Note that Eq. (22) is deduced from a many-pole plasmon model of the ELF using the quadratic dispersion relation, Eq. (20), for $E_i(q)$, and a constant damping coefficient, i.e., by setting $\Gamma_i(q) \approx \Gamma_i(0)$.

In Fig. 3, we present the inelastic DCS (in arbitrary units) over the 0-100 eV energy-loss range calculated from the above approaches (Eqs. (17)–(22)), for 100 eV, 500 eV, 1 keV, and 10 keV electrons. Since it is only the spectral distribution of the DCS that matters for sampling the energy loss, the depicted DCS have been normalized to their peak value for better visualization. We have also included for comparison the numerical Born results calculated directly from Eq. (16) using the dispersion relations Eqs. (19)–(21). Evidently, the effective-q approximation is in much better

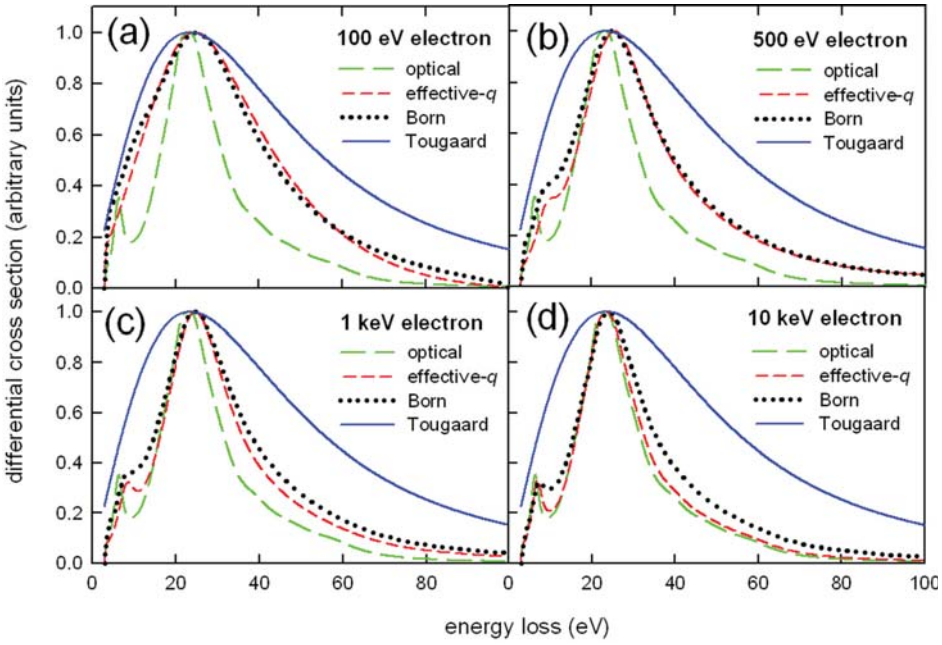

FIG. 3. Peak-normalized differential cross section (DCS) for energy-loss in inelastic scattering in MWCNT materials for 100 eV (panel a), 500 eV (panel b), 1 keV (panel c), and 10 keV (panel d) incident electron energies. Calculations are based on the Born approximation, Eq. (16) (dotted line), the optical approximation, Eq. (17) (long dash line), the effective-q approximation, Eqs. (18)–(21) (short dash line), and Tougaard's universal function, Eq. (22) (full line).

agreement with the Born calculations than the optical approximation, especially for low-energy electrons (sub-keV). On the other hand, Tougaard's universal function predicts a much broader distribution, although its peak position is in rather good agreement with the more elaborate models.

In principle, the ELF can be used for sampling both the discrete energy losses and the angular deflection (or, equivalently, the momentum transfer) in inelastic scattering through the doubly differential cross section $\frac{d^2\sigma_{inel.}}{dEdq}$. However, due to the formidable task of sampling from multi-variant distributions, as well as because the momentum transfer in inelastic scattering is, on average, much smaller than in elastic scattering, we follow the common practice to disregard the correlation between E and q. Then, it suffices to sample the inelastic scattering angle from the following simple expressions that are deduced from classical collision theory:[23]

$$\theta_{\text{prim}} = \sin^{-1}\left(\frac{2\,W_r}{2+\mu-\mu W_r}\right)^{1/2}, \tag{23a}$$

$$\theta_{\text{sec}} = \sin^{-1}\left(\frac{1-W_r}{1+\mu W_r/2}\right)^{1/2}, \tag{23b}$$

where θ_{prim} and θ_{sec} are the scattering angles of the primary and secondary electrons, respectively, with $W_r = E/T$ and $\mu = T/mc^2$.

The inelastic TCS in the Born approximation is formally obtained by integration of Eq. (16) over energy loss

$$\sigma_{inel} = \int_{E_{\min}}^{E_{\max}} \frac{d\sigma_{inel}}{dE}\,dE, \tag{24}$$

where the lower limit of integration, $E_{\min}$, equals either the ionization threshold (in the case of inner shells) or the band-gap. The upper limit of integration in Eq. (24) is set, as usual, at $E_{\max} = \min\{(T+E_{\min})/2,\, T-E_{\text{F}}\}$; however, in the present energy range, the first condition is always more restrictive than the second. The implementation of the (numerical) Born data, as obtained from Eq. (24), is generally straightforward since one needs to sample from a single table of σ_{inel} vs. T. However, to facilitate their use in subsequent computations, it is desirable to represent them analytically. Therefore, we have parameterized our σ_{inel} data of Eq. (24) by a Bethe-like analytic expression of the form:[59]

$$\sigma_{\text{Bethe}} = \frac{Z}{2\pi\, a_{\text{B}} N}\beta\, T^{-1}\ln(\gamma\, T), \tag{25}$$

where β and γ are material parameters that depend upon the ELF; for MWCNTs, the values $\beta = 27.9\,\text{eV}$ and $\gamma = 0.0588\,\text{eV}^{-1}$ have been obtained[60] with T in eV. Since Eq. (25) is a first-order expansion in T^{-1}, it eventually overestimates the Born results at low energies, as it can be clearly seen in Fig. 4. Therefore, to extend the usage of Eq. (25) down to 50 eV, we have employed a "corrected" Bethe model, which reads

$$\sigma_{inel} = \begin{cases} \sigma_{\text{Bethe}}, & T \geq 500\,\text{eV}, \\ \dfrac{\sigma_{\text{Bethe}}}{f_{\text{Bethe}}^{\text{corr.}}}, & T < 500\,\text{eV}, \end{cases} \tag{26}$$

where σ_{Bethe} refers to Eq. (25) and $f_{\text{Bethe}}^{\text{corr.}}$ is a fitting function that "corrects" Eq. (25) at low energies as follows:

$$f_{\text{Bethe}}^{\text{corr.}} = \frac{\sigma_{\text{Bethe}}}{\sigma_{\text{Born}}} \approx \frac{1-0.0354\,T}{-0.7655-0.0317\,T} \tag{27}$$

with T in eV. As it can be seen from Fig. 4, using Eqs. (25)–(27), an agreement to better than ±3% is achieved with the numerical Born results of Eq. (24) throughout the entire energy range of interest here.

Although the above inelastic scattering models explicitly consider polarization effects (through the dielectric

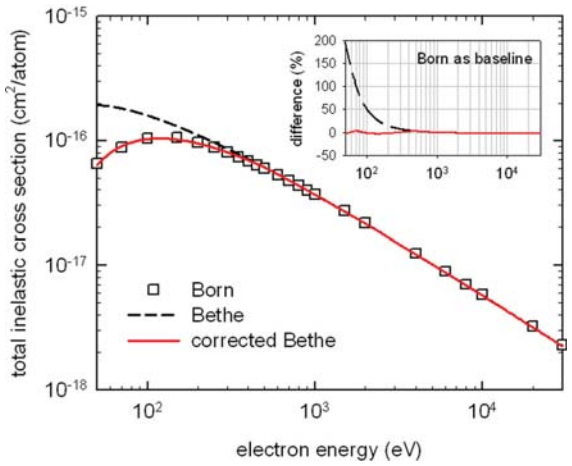

FIG. 4. Total cross section (TCS) for inelastic electron scattering in MWCNTs as a function of energy. Calculations are based on the Born approximation Eq. (24) (box symbols), the Bethe-like expression Eq. (25) (dash line) and the corrected Bethe model of Eqs. (26) and (27) (full line). The inset presents the % difference from the Born values.

response function), the lack of exchange (and correlation) corrections in the screened electron–electron interaction compromises their accuracy below ~200 eV. Schemes to correct for exchange in inelastic scattering are available.[29] However, they are all based on high-energy approximations which have limited justification below a few hundred eV.[61]

The above scattering models have been implemented in our homemade MC code[62,63] which simulates in an event-by-event mode electron trajectories in materials. As it is common in such "analogue" codes,[64] the target atoms are distributed randomly in the transport medium which is assumed to be homogeneous and isotropic. Within this approximation, particle transport scales linearly with the mass density of the material; as an example, the mean free path, λ, which is used to determine the distance-to-the-next-interaction is obtained via the standard expression $\lambda = \frac{A}{\rho N_A \sigma}$, where $\sigma = \sigma_{ela} + \sigma_{inel}$ is the total cross section per atom, A is the atomic weight, N_A is the Avogadro number, and ρ is the mass density of the medium. However, at least at the level of inelastic scattering, we go beyond the simple additivity rule of atomic cross sections by considering *non-linear* density effects arising from the long-range (longitudinal) polarization of the medium (also called "zero-energy" density effect)[44] through the dielectric response function.[64] On the other hand, the effects of inhomogeneity in the material, which may arise from the fact that there is potentially a lot of empty space in-between the nanotubes, or of anisotropy due to an internal ordering of nanotubes (e.g., in a forest), cannot be explicitly accounted for within the present methodology. However, in the present energy range, the electron mean free path (~1-50 nm) is much smaller than the linear dimensions of the transport medium considered in the simulations. Therefore, electron transport falls in the multiple-scattering (or diffusive) regime where, to a first approximation, the effects of inhomogeneity and anisotropy are averaged out and the use of a dielectric response function determined from bulk-like MWCNT data is well justified. As noted earlier, however, for *thin* MWCNTs (less than ~15 walls) or for well-aligned MWCNT samples with linear dimensions much smaller than ~50 nm, our scattering models should be considered only qualitative.

III. RESULTS AND DISCUSSION

A. Penetration parameters

The different scattering models described in the previous section have been used to calculate by MC simulation fundamental transport parameters of electron penetration in MWCNT materials such as the path length, the absorption depth, and the axial and lateral penetration depths. These parameters are essential in electron microscopy since they define the so-called irradiation or charge-carrier generation volume. Identifying the incident electron direction with the z-direction, its starting point at $(x_0, y_0, z_0) = (0, 0, 0)$, and the primary electron track with the set of coordinates $\{(x_i, y_i, z_i)\,;\, i = 1, ..., n\}$, where n is the total number of collisions experienced by the primary electron, the above penetration measures can be formally defined as follows: the path length is the average value of $r_{\text{total}} = \sum_{i=1}^{n} |\vec{r}_i|$, where $\vec{r}_i$ is the vector that connects two successive collisions with coordinates $(x_{i-1}, y_{i-1}, z_{i-1})$ and (x_i, y_i, z_i); the absorption depth is the average value of the z-coordinate of the *final* interaction point $z_{\text{final}} \equiv z_n$; the axial penetration depth is the average value of the z coordinate of the interaction point with the largest z coordinate, $z_{\max} = \text{Max}\{z_i\,;\, i = 1, ..., n\}$; and the lateral penetration depth is the average value of the radial distance of the interaction point with the largest *radial* distance from the incident beam direction $p_{\max} = \text{Max}\{(x_i^2 + y_i^2)^{1/2}; i = 1, ..., n\}$. By definition, z_n is always smaller than or equal to $z_{\max}$. Note also that r_{total}, z_{final}, $z_{\max}$, and $p_{\max}$, refer to a *single* primary electron while their averages ($\bar{r}_{\text{total}}$, $\bar{z}_{\text{final}}$, $\bar{z}_{\max}$, $\bar{p}_{\max}$) are taken over the total number of primary electrons simulated (here 100,000). For all simulations, the transport cut-off was set at 50 eV.

In Fig. 5, we present MC results for the path length, the absorption depth, the axial penetration depth, and the lateral penetration depth, calculated using the NISTelaFit model for elastic scattering (Eqs. (12)–(15)), hereafter denoted as model, and the effective-q approximation for inelastic scattering (Eqs. (18)–(21)). Since, in practice, MWCNT samples can have large variations in mass density, the results presented are density-normalized to facilitate their use in different applications. Note that the validity of the linear density scaling implied in the above normalization is conditioned to the discussion at the end of Sec. II A. It can be seen that for energies above ~400 eV, we have $\bar{r}_{\text{total}} > \bar{z}_{\max} > \bar{p}_{\max} > \bar{z}_{\text{final}}$. Interestingly, at very low energies (below ~400 eV), the penetration in the lateral direction is larger than in the axial direction, i.e., $\bar{p}_{\max} > \bar{z}_{\max}$, due to strong scattering at very low energies. Note also that the axial penetration depth, $\bar{z}_{\max}$, is about 8–15% larger than the absorption depth, $\bar{z}_{\text{final}}$ (often used as a measure of the penetration capacity of the beam), with their difference decreasing as the energy rises. The ratio of the absorption depth (or penetration depth) to the path length $\frac{\bar{z}_{\text{final}}}{\bar{r}_{\text{total}}}$ (or $\frac{\bar{z}_{\max}}{\bar{r}_{\text{total}}}$) is commonly called the *detour factor*, because it is a measure of the overall deviation from a straight-line trajectory. It can be seen from panel b that the detour factor

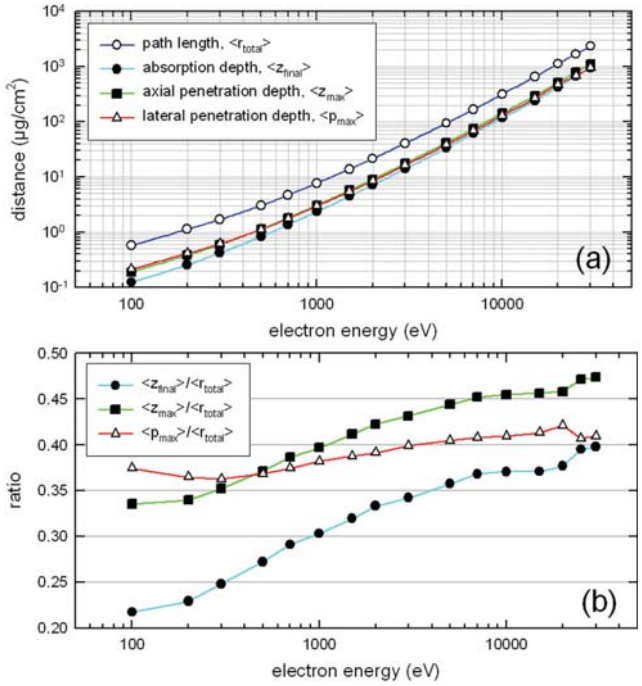

FIG. 5. Monte Carlo simulation results of the density-normalized path length ($\bar{r}_{\text{total}}$), absorption depth ($\bar{z}_{\text{final}}$), axial penetration depth ($\bar{z}_{\max}$), and lateral penetration depth ($\bar{p}_{\max}$) in MWCNT material as a function of electron energy (panel a), and the ratios $\frac{\bar{z}_{\text{final}}}{\bar{r}_{\text{total}}}$, $\frac{\bar{z}_{\max}}{\bar{r}_{\text{total}}}$, $\frac{\bar{p}_{\max}}{\bar{r}_{\text{total}}}$ (panel b). Electron transport is based on the NISTelaFit model for elastic scattering and the effective-q approximation for the inelastic scattering (see text for more details).

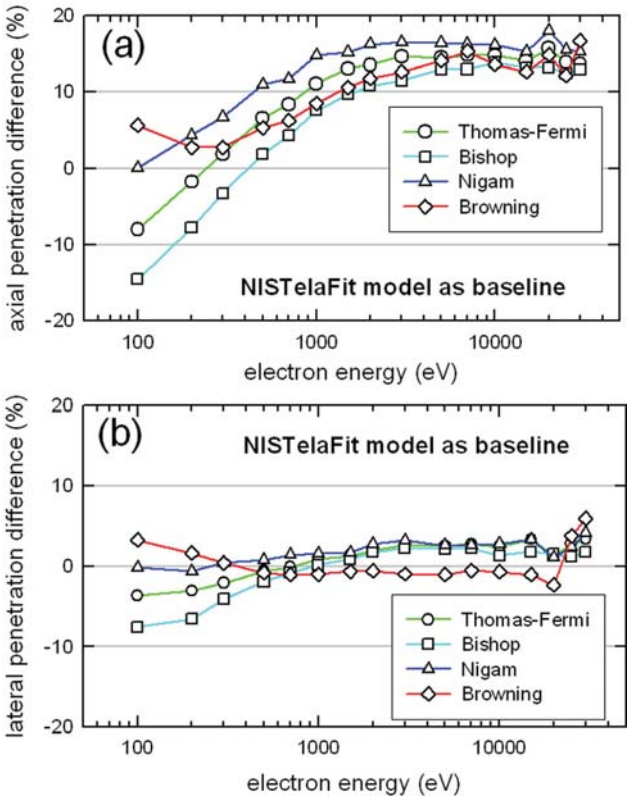

FIG. 6. Monte Carlo simulation results (expressed as percentage %) for the axial (panel a) and lateral (panel b) penetration depths for the different elastic models with the NISTelaFit model used as the baseline for the comparison. In these simulations, the inelastic model was kept the same.

increases with electron energy due to reduced (and more forward) scattering at high energies. In contrast, as the energy decreases, not only do the elastic interactions dominate over the inelastic ones but also the angular deflections in the inelastic collisions increase according to $\theta_{\text{prim}} \sim E/T$. The saturation behavior seen at high energies is because the relative contribution of elastic and inelastic scattering cross sections levels off. Note that the results of Fig. 5 are, on average, 20% higher than our earlier simulations,[26] which used the original Browning model[27] for elastic scattering. Compared to its later version[16] (used here), the original Browning model[27] favors the isotropic more than the Rutherford distribution, thus, predicting an overall smaller beam penetration.

In Fig. 6, we compare the axial (panel a) and lateral (panel b) penetration depths obtained from the different *elastic* scattering models (see Sec. II A), namely, the screened Rutherford model with the Thomas-Fermi, Bishop and Nigam screening parameter, the Browning model, and our NISTelaFit model; the latter was used as reference in the comparison. To isolate the effect of elastic scattering, in all simulations depicted in Fig. 6, the discrete-energy-loss model was based on the effective-q approximation. It can be seen from panel a that, compared to the NISTelaFit model, the screened Rutherford and Browning models predict up to ~20% larger axial penetration due to their (generally) smaller elastic TCS (see Fig. 1). The reason that the curves for the Thomas-Fermi and Bishop models turn negative below a few hundred eV is that their TCS at low energies becomes larger compared to the NISTelaFit model, thus, leading to less penetrating trajectories. On the other hand, since all the elastic models show fair agreement with respect to their transport cross section (Fig. 2), which reflects the average deflection in elastic scattering, their lateral penetration results exhibit much smaller differences, of the order of only a few %.

In Fig. 7, we compare the axial (panel a) and lateral (panel b) penetration depths for the different discrete-energy-loss models (see Sec. II B), namely, the optical approximation, the effective-q approximation, and Tougaard's universal function. The effective-q approximation, which shows the best agreement with the Born DCS values, was used as the baseline model for the comparison. To isolate the effect of the discrete-energy-loss model in the results of Fig. 7, the NISTelaFit elastic model was used for all the simulations. As we can see the optical approximation gives the largest penetration (both in the axial and lateral direction) over-estimating the effective-q approximation by 20–40% whereas Tougaard's universal function under-estimates it by 10–20%. These trends can be explained by the observation that the optical approximation tends to favor small energy losses whereas Tougaard's universal function large energy losses (see Fig. 3). As a result, the effective-q approximation leads to penetration values somewhere in-between the other two models. Notice that differences in penetration between the models gradually vanish at 100 eV due to the very small number of inelastic collisions needed for the electrons to fall below the 50 eV cut-off, combined with the fact that all three inelastic models predict

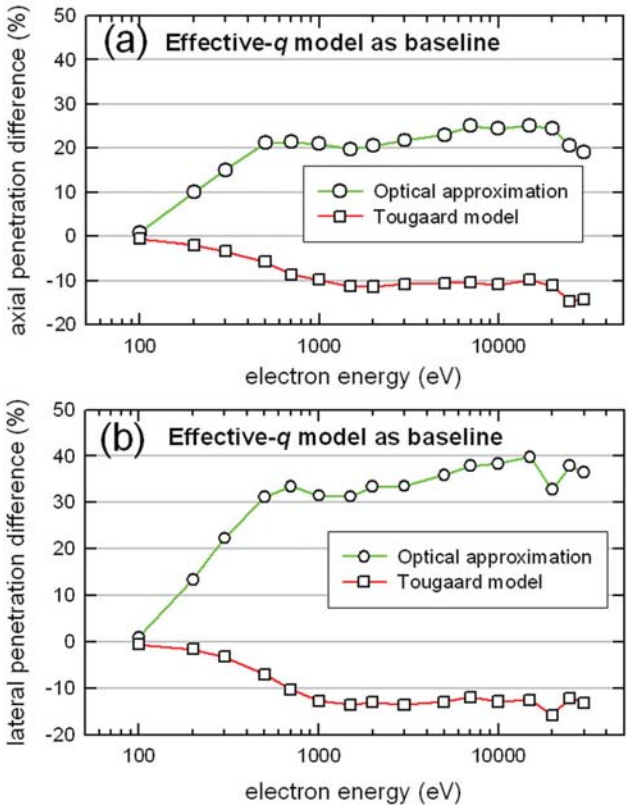

FIG. 7. Same as Fig. 6 but for the different inelastic DCS models with the effective-q approximation as the baseline for the comparison. In these simulations, the elastic model (NISTelaFit) was kept the same.

roughly the same value for the most probable energy loss (their DCS have maxima at about the same energy-loss value).

From an inspection of Figs. 6 and 7, we can also conclude that the penetration of electrons in MWCNT materials exhibits, overall, greater sensitivity to the inelastic (rather than the elastic) models we have examined.

B. Backscattering

The backscattering of electrons from solid surfaces, besides being a fundamental physical process in understanding electron beam–matter interactions, plays a key role in many applications of SEM. According to common usage, backscattered electrons (BSE) are those primary electrons that exit the surface of the material with energy greater than 50 eV. Then, the backscattering coefficient or yield, Y, is simply defined as the ratio of the number of BSE to the primary electrons that are incident on the surface of an infinitely thick sample. Note that the choice of 50 eV is arbitrary since secondary electrons with energy above 50 eV may also exit from the surface and, thus, experimentally be also included in the measurement of Y. Although the number of such "high-energy" secondary electrons is generally small compared to the number of "true" BSE, they are considered in the present simulations to better resemble the experimental condition. Similar to the penetration simulations, 100,000 primary electrons were used in the MC simulations of the backscattering yield, Y.

There are some empirical formulae of the backscattering yield for a range of materials and incident energies. According to Hunger and Küchler,[65] the backscattering yield as a function of both the atomic number (Z) and the incident electron energy (T in keV) is

$$\mathrm{Y}(Z,T) = T^{m(Z)}C(Z), \tag{28a}$$

where

$$m(Z) = 0.1382 - \left(0.9211/\sqrt{Z}\right), \tag{28b}$$

and

$$C(Z) = 0.1904 - 0.2236\,(\ln Z) + 0.1292\,(\ln Z)^2 - 0.01491\,(\ln Z)^3. \tag{28c}$$

Another analytic expression due to Staub[66] for energies below 30 keV reads:

$$\mathrm{Y}(Z,T) = b(T)\left\{1 - \exp\left(-0.0066\,b(T)^{-5/2}Z\right)\right\}, \tag{29a}$$

where

$$b(T) = 0.40 + 0.065\ln T \tag{29b}$$

with T in keV. More recently, Cazaux[67] has proposed an empirical expression that for low-Z materials (Z < 20) reads:

$$\mathrm{Y}(T) = a\{1 + \exp(-bT)\} \tag{30}$$

with T in eV. For carbon (Z = 6), Cazaux suggests $\alpha = 8.4$ and $\mathrm{b} = 0.0006\,\mathrm{eV}^{-1}$ in Eq. (30).

In Fig. 8, we present the backscattering yield, Y, as a function of incident electron energy based on the different elastic models and the effective-q approximation for the discrete-energy-loss model (Eqs. (18)–(21)). Comparison is made with the analytic expressions (using Z = 6) of Hunger and Küchler, Eq. (28), Staub, Eq (29), and Cazaux, Eq. (30)

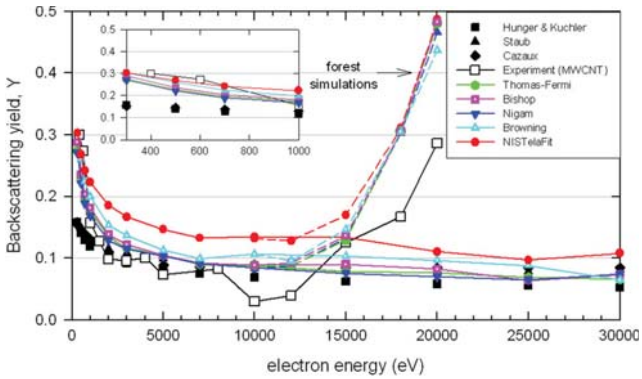

FIG. 8. Monte Carlo simulation of the backscattering yield, Y, as a function of incident electron energy using the effective-q approximation for inelastic scattering and different elastic scattering models (see text). Comparison is made with the empirical expressions (using Z = 6) of Hunger and Küchler,[65] Eq. (28), Staub,[66] Eq. (29), and Cazaux,[67] Eq. (30), as well as the experimental data for MWCNT forests.[21] The broken lines denote simulations for the experimental forest geometry (diameter of 500 μm and density of 0.019 g/cm^3). The inset depicts the sub-keV energy range.

as well as the recent experimental measurements on MWCNT forests[21] (cylindrically shaped arrays of vertically aligned MWCNTs, with a macroscopic diameter of 500 μm and density of 0.019 g/cm^3). For these experiments, the MWCNT forests were grown on silicon substrates using atmospheric-pressure chemical vapor deposition. Before the growth, circular patterns (with a diameter of 500 μm) of iron catalyst were created on the substrate using optical lithography, electron-beam deposition and lift-off. Vertically growing out of these catalyst circles to a height of about 1 mm, the nanotubes formed cylindrical arrays. To measure the backscattering yield, a forest was placed in a scanning electron microscope and illuminated by the primary beam on its top surface near the center (the electron beam was parallel to the axis of the cylindrical forest). The primary beam and stage currents were measured by a high-precision electrometer while a bias of +50 V on the specimen ensured that only electrons with more than 50 eV of kinetic energy (which we have defined as backscattered electrons) could escape. The emitted current (the current escaping the specimen into vacuum) was determined based on the primary beam and stage currents and knowing that, in steady state, any electron entering the specimen has to leave either through the stage or into vacuum. The backscattering yield was calculated as the ratio of the emitted current to the primary beam current. Note that, as discussed before, strictly speaking, a small number of high-energy secondary electrons (with a kinetic energy >50 eV) are also naturally included in this "backscattering" current, and that is why we have also included them in the simulations in order to have a fair comparison. The experiment was performed at different values of the primary beam energy. For more details, see Refs. 21 and 68.

In all cases, the backscattering yield increases with decreasing incident energy in the sub-keV range. This is a well-established behavior for low-Z materials and is opposite to the case of high-Z media where the backscattering yield declines with incident energy below a few keV. Interestingly, the experimental data for the MWCNT forests show a much steeper rise compared to the Z = 6 materials in the sub-keV range. This trend is well predicted by our study, with simulations employing the NISTelaFit model for elastic scattering and the effective-q approximation for inelastic scattering showing the best agreement with the forest data. Above ~5 keV, the backscattering yield is known to reach a plateau, which is also observed in the present results and the empirical expressions. However, the plateau range in the forest data extends over a rather limited energy range because of possible escape of electrons from the side-walls of the sample (as discussed elsewhere[68]). The latter effect results in the increase of Y for sufficiently high beam energies. The data of Fig. 5 agree with the experimentally observed onset of the sidewalls escape effect in the forest data at ~10-15 keV, where the lateral penetration of the beam becomes comparable to the radius of the forest. The additional simulations carried out for the geometry used in the forest experiments (and also shown in Fig. 8 with broken lines), clearly confirm the effect of the finite lateral dimensions of the forests on the backscattering yield measured in those experiments. In fact, at the highest beam energy used in the experiments (20 keV), our simulations predict an (average) lateral penetration for all elastic models of ~250 μm, which coincides with the forest radius. As a result, the contribution of the sidewalls escape electrons dominates over that of the "true" backscattering electrons, and all models predict roughly the same backscattering yield (~0.5). The lower yield (~0.3) measured at 20 keV can be explained by the fact that, experimentally, not all sidewalls escape electrons are counted. In these experiments, the backscattering yield was inferred by measuring the electron current that goes through the specimen stage. Then, using charge neutrality and knowing the primary beam current as well, it was determined how many electrons escape. So, some of the electrons escaping from the sidewalls could still have a forward momentum which would make them hit the silicon substrate and go through the specimen stage and thus not be counted as backscattered.[21]

With respect to the inelastic models (not shown in Fig. 8 for clarity), the backscattering yield as a function of beam energy for both the optical approximation and the Tougaard universal function exhibits the same trend as the effective-q approximation. However, the plateau value for the optical approximation, which predicts a smaller energy-loss rate, is ~30–40% higher whereas for the Tougaard model, which predicts a higher energy-loss rate, is ~10–20% lower. These results are in accord with the Vicanek-Urbassek backscattering theory[69] whereby the higher the energy-loss rate the smaller the backscattering yield for the same elastic scattering model.

IV. CONCLUSION

A Monte Carlo model of electron trajectories in MWCNT materials is presented using state-of-the-art scattering cross sections based on an analytic parameterization of the Mott cross sections of NIST and an optical-data model dielectric response function with a full dispersion. We show that, depending on the approximations used to compute elastic and inelastic electron scattering cross sections, penetration and backscattering characteristics may vary by typically 20–40% for beam energies relevant to SEM irradiation. The present simulations confirm the steep increase of the backscattering yield at sub-keV energies in recent experimental data on MWCNT forests, as well as the effect of the sidewalls escape of electrons at high beam energies. The ability of our Monte Carlo model to predict the experimental backscattering data of the forest of aligned MWCNTs over a broad energy range is considered to be a testimony to its generality and predictive power. Nevertheless, for small-size samples with internal ordering or for individual thin MWCNTs, the effect of inhomogeneity and anisotropy should be explicitly considered. Furthermore, as discussed, improvements on the scattering models below ~200 eV would be necessary for more reliable simulations at ultra-low beam energies and especially for secondary emission applications not considered here.

[1]A. Nojeh, B. Shan, K. Cho, and R. F. W. Pease, Phys. Rev. Lett. **96**, 056802 (2006).
[2]F. Banhart, Rep. Prog. Phys. **62**, 1181 (1999).

[3]A. V. Krasheninnikov and K. Nordlund, J. Appl. Phys. **107**, 071301 (2010).
[4]A. V. Krasheninnikov and F. Banhart, Nature Mater. **6**, 723 (2007).
[5]P. J. Boul, K. Turner, J. Li, M. X. Pulikkathara, R. C. Dwivedi, E. D. Sosa, Y. Lu, O. V. Kuznetsov, P. Moloney, R. Wilkins, M. J. O'Rourke, V. N. Khabashesku, S. Arepalli, and L. Yowell, J. Phys. Chem. C **113**, 14467 (2009).
[6]X. W. Tang, Y. Yang, W. Kim, Q. Wang, P. F. Qi, H. J. Dai, and L. Xing, Phys. Med. Biol. **50**, N23 (2005).
[7]K. Kostarelos, A. Bianco, and M. Prato, Nat. Nanotechnol. **4**, 627 (2009).
[8]M. Michan, P. Yaghoobi, B. Wong, and A. Nojeh, Phys. Rev. B **81**, 195438 (2010).
[9]M. Knupfer, T. Pichler, M. S. Golden, J. Fink, A. Rinzler, and R. E. Smalley, Carbon **37**, 733 (1999).
[10]M. Dapor, *Electron-Beam Interactions with Solids: Application of the Monte Carlo Method to Electron Scattering Problems* (Springer, New York, 2003).
[11]D. C. Joy, *Monte Carlo Modeling for Electron Microscopy and Microanalysis* (Oxford University Press, New York, 1995).
[12]R. Gauvin, E. Lifshin, H. Demers, P. Horny, and H. Cambell, Microsc. Microanal. **12**, 49 (2006).
[13]D. Drouin, A. R. Couture, D. Joly, X. Tastet, and V. Aimez, Scanning **29**, 92 (2007).
[14]N. W. M. Ritchie, Surf. Interface Anal. **37**, 1006 (2005).
[15]D. C. Joy and S. Luo, Scanning **11**, 176 (1989).
[16]R. Browning, T. Z. Li, B. Chui, J. Ye, R. F. W. Pease, Z. Czyiewski, and D. C. Joy, J. Appl. Phys. **76**, 2016 (1994).
[17]R. Gauvin and D. Drouin, Scanning **15**, 140 (1993).
[18]D. Drouin, R. Gauvin, and D. C. Joy, Scanning **16**, 67 (1994).
[19]M. Yasuda, H. Kawata, and K. Murata, J. Appl. Phys. **77**, 4706 (1995).
[20]Y. T. Yue, H. M. Li, and Z. J. Ding, J. Phys. D: Appl. Phys. **3**, 1966 (2005).
[21]M. K. Alam, P. Yaghoobi, and A. Nojeh, J. Vac. Sci. Technol. B **28**, C6J13 (2010)
[22]M. K. Alam and A. Nojeh, J. Vac. Sci. Technol. B **29**, 041803 (2011)
[23]R. Shimizu and Z.-J. Ding, Rep. Prog. Phys. **55**, 487 (1992).
[24]J. R. Lowney, Scanning **18**, 301 (1996).
[25]I. Kyriakou, D. Emfietzoglou, R. Garcia-Molina, I. Abril, and K. Kostarelos, Appl. Phys. Lett. **94**, 263113 (2009).
[26]I. Kyriakou, D. Emfietzoglou, R. Garcia-Molina, I. Abril, and K. Kostarelos, J. Appl. Phys. **110**, 054304 (2011).
[27]R. Browning, Appl. Phys. Lett. **58**, 2845 (1991).
[28]D. Emfietzoglou, I. Kyriakou, R. Garcia-Molina, I. Abril, and K. Kostarelos, Appl. Phys. Lett. **100**, 093113 (2012).
[29]J. M. Fernández-Varea, R. Mayol, D. Liljequist, and F. Salvat, J. Phys.: Condens. Matter **5**, 3593 (1993).
[30]Z.-J. Ding and R. Shimizu, Scanning **18**, 92 (1996).
[31]J.-Ch. Kuhr and H.-J. Fitting, Phys. Status. Solidi. A **172**, 433 (1999).
[32]C. J. Powell and A. Jablonski, J. Phys. Chem. Ref. Data **28**, 19 (1999).
[33]P. Hovington, D. Drouin, R. Gauvin, D. C. Joy, and N. Evans, Scanning **19**, 29 (1997).
[34]J. Baro, J. Sempau, J. M. Fernandez-Varea, and F. Salvat, Nucl. Instrum. Methods Phys. Res. B **100**, 31 (1995).
[35]A. Jablonski, F. Salvat, and C. J. Powell, *NIST Electron Elastic-Scattering Cross-Section Database – Version 3.0* (National Institute of Standards and Technology, Gaithersburg, MD, 2002).
[36]A. Jablonski, F. Salvat, and C. J. Powell, J. Phys. Chem. Ref. Data **33**, 409 (2004).
[37]J. M. Fernández-Varea, F. Salvat, M. Dingfelder, and D. Liljequist, Nucl. Instrum. Methods Phys. Res. B **229**, 187 (2005).
[38]B. P. Nigam, M. K. Sundaresan, and T. Y. Wu, Phys. Rev. **115**, 491 (1959).
[39]I. Adesida, R. Shimizu, and T. E. Everhart, J. Appl. Phys. **51**, 5962 (1980).
[40]L. Reimer and B. Lodding, Scanning **6**, 128 (1984).
[41]Z. Czyzewski, D. O. MacCallium, A. Romig, and D. C. Joy, J. Appl. Phys. **68**, 3066 (1990).
[42]H.-J. Fitting and J. Reinhardt, Phys. Status. Solidi. A **88**, 245 (1985).
[43]D. Pines, *Elementary Excitations in Solids* (Benjamin, New York, 1964).
[44]H. Nikjoo, S. Uehara, and D. Emfietzoglou, *Interaction of Radiation with Matter*, (CRC Taylor & Francis, Boca Raton, FL, 2012).
[45]Öztürk and W. Williams, J. Appl. Phys. **74**, 4723 (1993).
[46]C. J. Powell, Surf. Sci. **44**, 29 (1974).
[47]R. Kuzuo, M. Terauchi, and M. Tanaka, Jpn. J. Appl. Phys. **31**, L1484 (1992).
[48]R. H. Ritchie and A. Howie, Philos. Mag. **36**, 463 (1977).
[49]S. Tanuma, C. J. Powell, and D. R. Penn, J. Electron Spectrosc. Relat. Phenom. **62**, 95 (1993).
[50]C. T. Chantler, K. Olsen, R. A. Dragoset, J. Chang, A. R. Kishore, S. A. Kotochigova, and D. S. Zucker. Available at http://physics.nist.gov/ffast.
[51]D. Emfietzoglou, I. Kyriakou, I. Abril, R. Garcia-Molina, I. D. Petsalakis, H. Nikjoo, and A. Pathak, Nucl. Instrum. Methods Phys Res. B **267**, 45 (2009).
[52]J. -Ch. Kuhr and H.-J. Fitting, J. Electron Spectrosc. Related Phenom. **105**, 257 (1999).
[53]W. de la Cruz and F. Yubero, Surf. Interf. Anal. **39**, 460 (2007).
[54]J. D. Bourke and C. T. Chantler, J. Phys. Chem. A **116**, 3202 (2012).
[55]M. H. Upton, R. F. Klie, J. P. Hill, T. Gog, D. Casa, W. Ku, Y. Zhu, M. Y. Sfeir, J. Misewich, G. Eres, and D. Lowndes, Carbon **47**, 162 (2009).
[56]C. Yannouleas, E. N. Bogachek, and U. Landman, Phys. Rev. B **53**, 10225 (1996).
[57]S. Tougaard, Solid State Commun. **61**, 547 (1987).
[58]S. Tougaard, Surf. Interf. Anal. **25**, 137 (1997).
[59]C. J. Powell, Surf. Interf. Anal. **7**, 263 (1985).
[60]D. Emfietzoglou, I. Kyriakou, R. Garcia-Molina, I. Abril, and K. Kostarelos, J. Appl. Phys. **108**, 054312 (2010).
[61]D. Emfietzoglou and H. Nikjoo, Radiat. Res. **163**, 98 (2005).
[62]D. Emfietzoglou, G. Papamichael, and M. Moscovitch, J. Phys. D: Appl. Phys. **33**, 932 (2000).
[63]A. Akkerman, J. Barak, and D. Emfietzoglou, Nucl. Instrum. Methods Phys Res B **227**, 319 (2005).
[64]F. Salvat and J. M. Fernández-Varea, Metrologia **46**, S112 (2009).
[65]H.-J. Hunger and L. Kuchler, Phys. Status Solidi A **56**, K45 (1979).
[66]P.-F. Staub, J. Phys. D: Appl. Phys. **27**, 1533 (1994).
[67]J. Cazaux, J. Appl. Phys. **112**, 084905 (2012).
[68]M. K. Alam, P. Yaghoobi, and A. Nojeh, Scanning **31**, 221 (2009).
[69]M. Vicanek and H. M. Urbassek, Phys. Rev. B **44**, 7234 (1991).